J Sol-Gel Sci Technol (2015) 73:227–241
DOI 10.1007/s10971-014-3521-3

ORIGINAL PAPER

Optimizing sol–gel synthesis of magnesia-stabilized zirconia (MSZ) nanoparticles using Taguchi robust design for thermal barrier coatings (TBCs) applications

Morteza Hajizadeh-Oghaz · Reza Shoja Razavi · Mohammad Khajelakzay

Received: 8 April 2014 / Accepted: 19 September 2014 / Published online: 1 October 2014

Abstract Nanocrystalline magnesia-stabilized zirconia powders have been synthesized using Pechini method and Taguchi experiment design. In the present research work, Taguchi method was applied to investigate the effect of citric acid to ethylene glycol mole ratio (CA/EG), citric acid to transition metal mole ratio (CA/TM), calcination temperature and time on particle size. CA/EG and CA/TM were determined to be the main parameters controlling particle size of magnesia-stabilized zirconia powders. Under optimum conditions, a verification experiment was carried out, and the average primary particle size of magnesia-stabilized zirconia powders was found to be 5.6 nm with homogeneous particle size distribution. Contribution percentage of each manageable factor was also determined. Furthermore, characterization of optimum sample was accomplished by means of thermogravimetric analysis, differential thermal analysis, X-ray diffraction, transmission electron microscopy, field emission scanning electron microscope and Raman spectroscopy.

Keywords Nanostructured materials · Pechini method · Sol–gel process · Magnesia-stabilized zirconia · Taguchi design

1 Introduction

Thermal barrier coatings (TBCs) have shown a significant potential to develop the permanence and efficiency of gas engines [1]. Much attention is now being paid to zirconia-based thermal barrier coatings owing to their inherent capability of providing higher thermal efficiencies to fossil-fuel-fired energy conversion systems [2]. Pure zirconia is transformed from tetragonal to monoclinic phase and thus volumetric changes are associated with this transformation when temperature is changed. This transformation is not desirable in the application of thermal barrier coatings. Therefore, it can be stabilized with either CaO (5 wt%), MgO (15–24 wt%) or Y_2O_3 (6–12 wt%) [3–5]. Magnesia-stabilized zirconia (MSZ) ceramic powders have been extensively used for more than 30 years to protect sheet metal combustor, resist the effects of molten copper or aluminum on various types of molds and troughs, resist particle erosion at temperatures of about 845 °C (1,550 °F) on missile nose cones, and serve as thermal barrier on brazing and heat treating, and coatings on tuyeres for iron forging or refining operations. However, Pratt and Whitney used MgO stabilised zirconia TBCs on burner cans in 1963 [4]. Among different materials, ZrO_2–MgO ceramic powder is relatively cheaper than ZrO_2–Y_2O_3. That is why it is utilized in those regions where the temperature intensity is relatively low, e.g., in the exhaust of the jet engines. Further, an MgO stabilized system can be used for the development of an intermediate coating in a three-part graded coating system with magnesium zirconate as a top-coat [6]. Furthermore, on the basis of reaction [7], MgO-stabilized ZrO_2 would be expected to be more resistant to vanadium fuel impurities than YSZ; and this appears to have been found in marine engine service [8]. Creation of nanostructure materials is a promising approach to yield modern TBCs. In recent years, nanostructured zirconia based TBCs deposited by atmospheric plasma spraying have received considerable attention because of some astonishing properties not found in their conventional counterparts [9].

Particle size of magnesia-stabilized zirconia is an important parameter, because the thermal conductivity

M. Hajizadeh-Oghaz (✉) · R. Shoja Razavi · M. Khajelakzay
Department of Materials Science and Engineering, Maleke Ashtar University of Technology, Shahinshahr, Iran
e-mail: Hajizadeh@mut-es.ac.ir

intensely depends on the size of agglomerated nanoparticles [10, 11]. However, to the best of our knowledge, most studies have been focused on the synthesis of state-of-the-art YSZ nanoparticles to control particle size, and particle size distribution, but very few studies have dealt with the synthesizing and controlling the particle sizes of MSZ nanoparticles for the thermal barrier coatings applications. According to the promising advantages of nanostructured TBCs materials mentioned above, a comprehensive study seems to be necessary for optimizing the fabrication of this material. Recently, a number of methods have been used to synthesize magnesia-stabilized zirconia nanoparticles, such as alkoxide sol–gel processing [12], in situ peptisation of co-precipitated oxalate gel [13], citrate method [14, 15], Pechini type sol–gel method [16] and Liquid Precursors processes [17]. In this study, among these methods, Pechini method was used because it made it relatively easy to produce nanoparticles.

In Pechini sol–gel process, an alpha-hydroxycarboxylic acid such as citric acid is used to chelate with various cation precursors forming a polybasic acid. In the presence of a polyhydroxy alcohol, such as ethylene glycol, these chelates will react with the alcohol to form organic esters and water. By heating the mixture, polyesterification occurs, yielding a homogeneous sol; metal ions are found to be uniformly distributed throughout the organic matrix in that sol. The crystallization occurs simultaneously with the elimination of the organic matter in a subsequent thermal treatment, giving rise to a crystalline material with high chemical and structural homogeneity [18].

Taguchi method used in orthogonal array experimental design can be employed to handle any given system by a set of independent variables over specific levels. This method not only saves time and money, but also leads to a strong and more fully developed process by providing a simple, systematic and efficient methodology for the optimization of the optimum design parameters with only a few well-defined experimental samples [19, 20]. Many researchers have investigated particle size optimization of different nanoparticles by means of Taguchi method [19–34]. In this study, particle size prediction possibility of magnesia-stabilized zirconia nanoparticles was investigated and a modified synthesis method was presented for decreasing the particle size of magnesia-stabilized zirconia nanoparticles.

2 Materials and methods

2.1 Synthesis of MgO–ZrO_2 nanopowders

MgO–ZrO_2 nanopowders were prepared by Pechini sol–gel method. $ZrOCl_2{\cdot}8H_2O$ (Nornik Chemicals, Russia), and $Mg(NO_3)_2{\cdot}6H_2O$ (AR Grade, CDH Chemicals, India) were chosen as the starting materials because of their high solubility in water. Citric acid and ethylene glycol were used as the chelating and esterification agents, respectively. Double distilled water was also used throughout the experiment as solvent.

Solutions of $ZrOCl_2{\cdot}8H_2O$, $Mg(NO_3)_2{\cdot}6H_2O$ (corresponding to 24 wt% of MgO and 76 wt% of ZrO_2 in the final oxide powder) were prepared by slowly adding the respective salts in a constantly stirred water containing glass beaker. The prepared solutions of $ZrOCl_2{\cdot}8H_2O$ and $Mg(NO_3)_2{\cdot}6H_2O$ were well mixed in a glass beaker using a magnetic stirrer and hot plate. Then, the citric acid solution and ethylene glycol were added into the stirred mixed cation solutions, thereby yielding a colorless solution that was allowed to settle down at the temperatures of 100, 200 and 300 °C, each for 2 h. All these precursors were oven dried at 250 °C until water and other organics were evaporated. The resultant burned gel was calcinated in a furnace at different temperatures and times according to M_{16} array of Taguchi experiment design. The flow chart of the proposed integrated approach is shown in Fig. 1. Figure 2 illustrates the chemical reactions involved in this process and presents one feasible structure of the polymer.

2.2 Design of experiments

Taguchi M_{16} statistical design [35, 36] was utilized to investigate the effective factors on sol–gel synthesis of magnesia-stabilized zirconia nanoparticles and optimize the preparation condition. M_{16} is an orthogonal array of experiments, designed in a manner to fulfill 4 and 3-level factors based on Taguchi experiment designs. The four important factors studied based on the preliminary tests and literature surveys were: citric acid to ethylene glycol mole ratio (CA/EG), citric acid to transition metal mole ratio (CA/TM), calcination temperature and time [37–41]. The second step was determination of levels for each factor (Table 1). The structure of Taguchi's orthogonal robust design and the results of measurement are shown in Table 2. Furthermore, in the present study, the Qualitek-4 (w32b) software was used for the design of experiments by Taguchi method.

2.3 Characterization of powders

The powders were characterized by X-ray diffraction (XRD). It was performed on calcined powders for phase characterization, with Ni filtered Cu-Kα radiation (0.15406 nm) and working power of 40 kV and 40 mA in the 2θ range of 20–90, on a X-ray diffractometer (XRD; Bruker D8 Advance, Germany). The microscopic features of the samples were characterized by field emission scanning electron microscopy (FESEM; S-4160, Hitachi Ltd.,

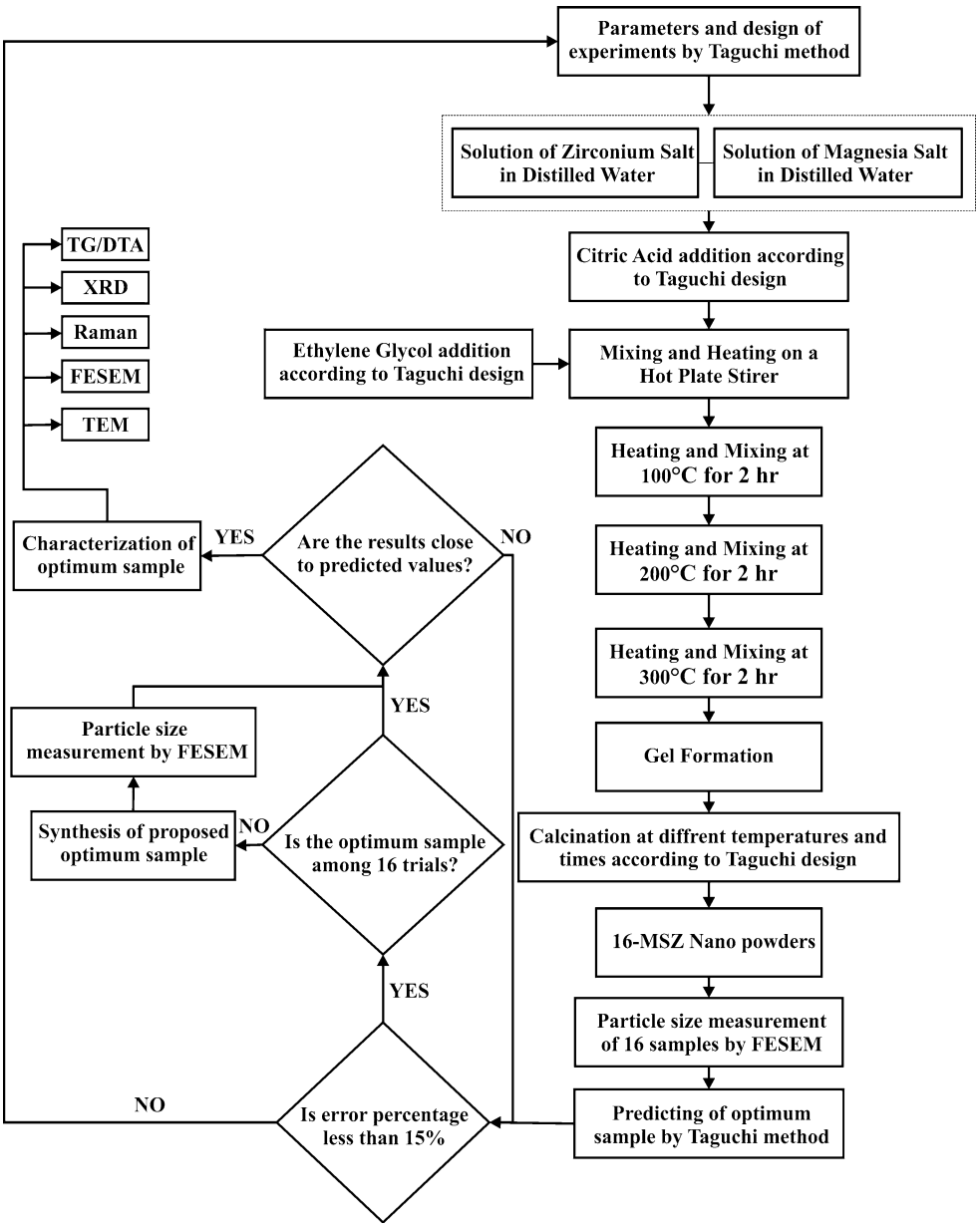

Fig. 1 Flowchart for preparing MSZ powders by Pechini method

Japan) with an accelerating voltage of 15 kV. A thin gold coating was evaporated onto the surface of specimens for electrical conductivity before microscopic observations. Transmission electron microscopy (TEM) micrographs were obtained using a CM200 Philips electron microscope (200 kV). Samples were prepared by diluting about 1 mg powder in 10 ml ethanol and then applying a drop of the solution on carbon coated copper grid. Particle size and size distribution were determined using the image tool software. The gel precursor was characterized by thermal analysis (TG/DTA) in static atmosphere air between 30 and 900 °C, with a heating rate of 5 °C min^{-1}, using 7.5 mg of the sample in Pt crucible. The calcined powders were characterized by Raman spectroscopy (BRUKER (Germany) Model: SENTERRA (2009)) with a CCD detector cooled by liquid nitrogen; the 785 nm line of an Ar^{+} laser was used as the excitation. The spectra were collected at 25 °C in spectral range of 100–800 cm^{-1} and source resolution of 3–5 cm^{-1} with a laser power of 50 mW.

Thermal diffusivity α(T) measurements were carried out with laser flash apparatus Theta (Theta Industries Inc., Port Washington, NY, USA) in vacuum (<0.01 Pa). Measurements were performed at seven different temperatures in the temperature range of 100–1,300 °C. Prior to evaluating the thermal diffusivity, in order to make the sample surfaces opaque, thin layers of colloidal graphite were painted on both the front and the back faces.

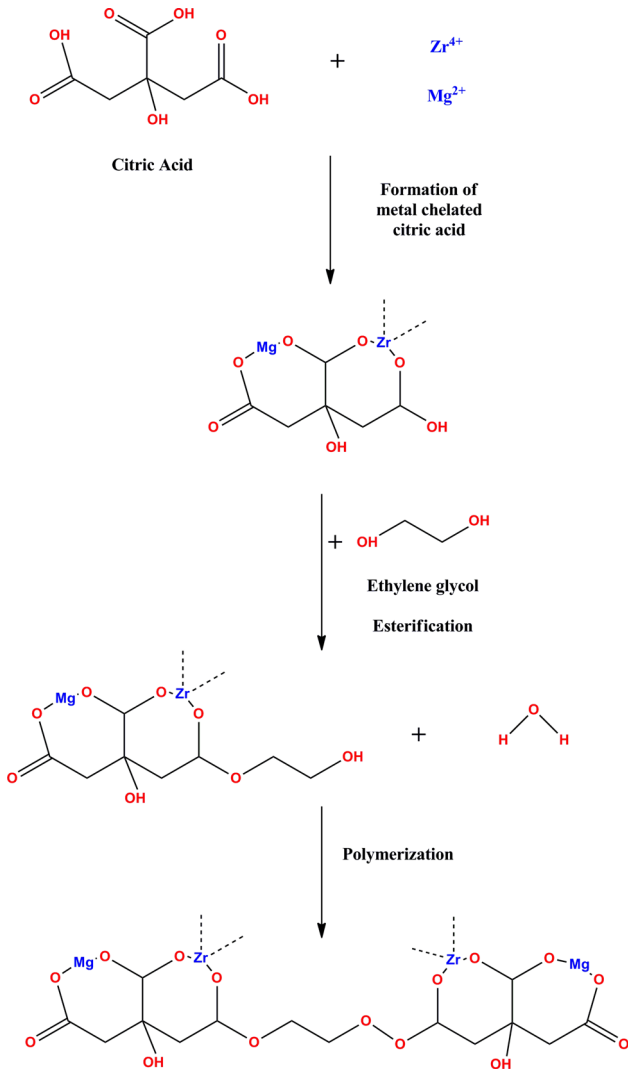

Fig. 2 Schematic illustration showing the solution chemistry and reactions involved in the Pechini process

Table 1 Parameters and levels for Taguchi design

Factor	Representation	Level 1	Level 2	Level 3	Level 4
CA/EG	A	1	2	3	4
CA/TM	B	1	2	3	4
Calcination temperature (°C)	C	600	700	800	900
Calcination time (h)	D	4	6	8	–

Thermal conductivities k(T) were calculated using the equation $k(T) = \alpha(T) \times C_P(T) \times \rho_B$ where ρ_B is the bulk density of the coating. Thermal conductivity values were calculated in 50 °C intervals at temperature range of 150–1,250 °C. For these temperature points the thermal diffusivity data was interpolated from the original data.

Table 2 Experiment factors, levels and particle size of the synthesized MSZ powders

Experiment no.	CA/EG	CA/TM	Calcination temperature (°C, ±5)	Calcination time (h)	Average particle size (nm, ±1)
1	1	1	600	4	17
2	1	2	700	6	19
3	1	3	800	8	14
4	1	4	900	4	21
5	2	1	700	8	22
6	2	2	600	4	20
7	2	3	900	4	19
8	2	4	800	6	30
9	3	1	800	4	32
10	3	2	900	8	20
11	3	3	600	6	34
12	3	4	700	4	38
13	4	1	900	6	20
14	4	2	800	4	27
15	4	3	700	4	30
16	4	4	600	8	31
Total	40	40	40	28	

3 Results and discussion

3.1 Particle size and morphology of nanoparticles

According to the M_{16} design proposed by the Taguchi manner, particle size of MSZ nanoparticles was estimated from Field emission electron microscopy (FE-SEM) images. Figures 3 and 4 illustrate the agglomerate structures of MSZ powders for 16 samples synthesized at different conditions according to the Taguchi design. Image tool software was used to assess the average particle size of these different 16 trials. Table 2 represents calculated particle size for each of 16 samples.

3.2 Crystal structure identification

Powder XRD analysis was performed on 16 samples and were shown in Figs. 5a–h and 6a–h. In some cases, only a combination of cubic ZrO_2 and cubic MgO peaks was found, while in others, a mixture of cubic and monoclinic zirconia and cubic MgO was determined (Fig. 5b, e); also, in the case of sample 10 (Fig. 6b), a mixture of both tetragonal zirconia and cubic magnesia was present. These

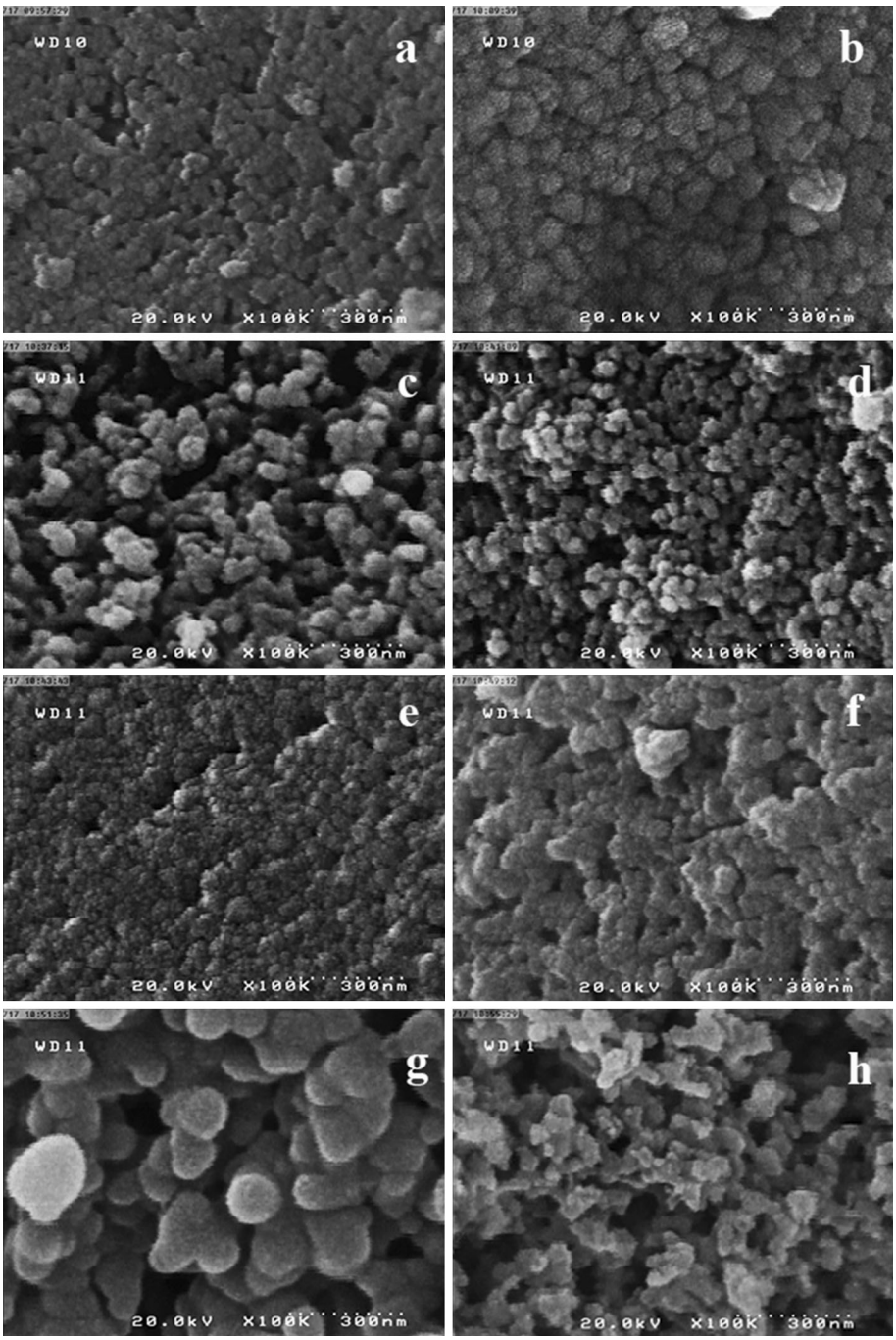

Fig. 3 Field emission electron microscopy of samples **a** sample 1, **b** sample 2, **c** sample 3, **d** sample 4, **e** sample 5, **f** sample 6, **g** sample 7 and **h** sample 8

results indicated that stabilization process of high temperature cubic crystal structure was done successfully.

The first achievement in thermal barrier coatings was attained by plasma-sprayed coatings, of magnesia-stabilized zirconia (MSZ) containing 25 wt% MgO, which contained a 100 % cubic crystal structure [42]. Nonetheless, the different equilibrium diagrams drawn for the ZrO_2–MgO system showed that the equilibrium phases were at temperatures <1,400 °C, either monoclinic or tetragonal zirconia plus MgO (Fig. 7) [43]. Nonetheless, feedstock powder could not be in a 100 % cubic crystal structure form, because after atmospheric plasma spray, due to rapid solidification, a metastable cubic crystal structure of zirconia would be formed. Therefore, in the as sprayed condition, this single cubic phase is principally a metastable phase. When coatings of the magnesia-stabilized zirconia were thermally cycled between 20 and 1,200 °C, the thermal diffusivity was gradually increased with each cycle [44]. These increases were owing to the precipitation, from the solid solution and of the stabilizing

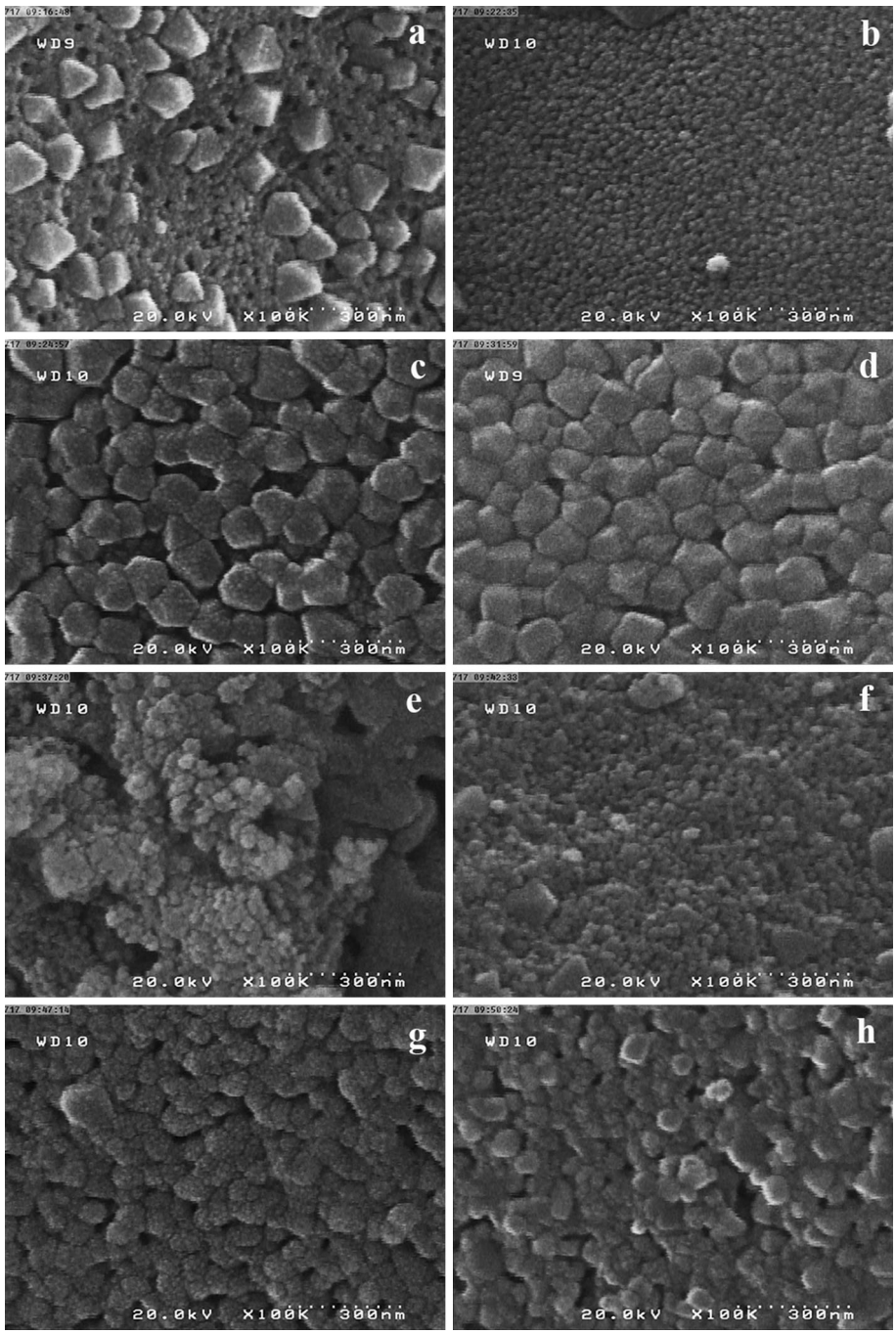

Fig. 4 Field emission electron microscopy of samples **a** sample 9, **b** sample 10, **c** sample 11, **d** sample 12, **e** sample 13, **f** sample 14, **g** sample 16 and **h** sample 16

oxide. Precipitation in the neighborhood of inter-splat boundaries in ZrO_2–MgO alloys has been reported [44].

As illustrated in Fig. 8, the equilibrium crystalline materials have been brought from a free energy, G_0, into a highly non-equilibrium (metastable) state, with a free energy, G_1, by the process of energization. This could be attained by certain external dynamic forcing, e.g., through the increase of temperature T (melting or evaporation), irradiation, the use of pressure P, or the storage of mechanical energy E by plastic deformation. Such energized materials have been referred to as ''driven materials'' by Martin and Bellon [45]. Also, the energization usually includes a likely alteration of state from solid to liquid (melting) or gas (evaporation). For instance, in rapid solidification processing, the starting solid material is melted and the material is vaporized throughout vapor deposition. The energized material is then ''quenched'' into a configurationally solid state by methods such as rapid solidification processing or mechanical alloying, such that the subsequent phase is in an extremely metastable

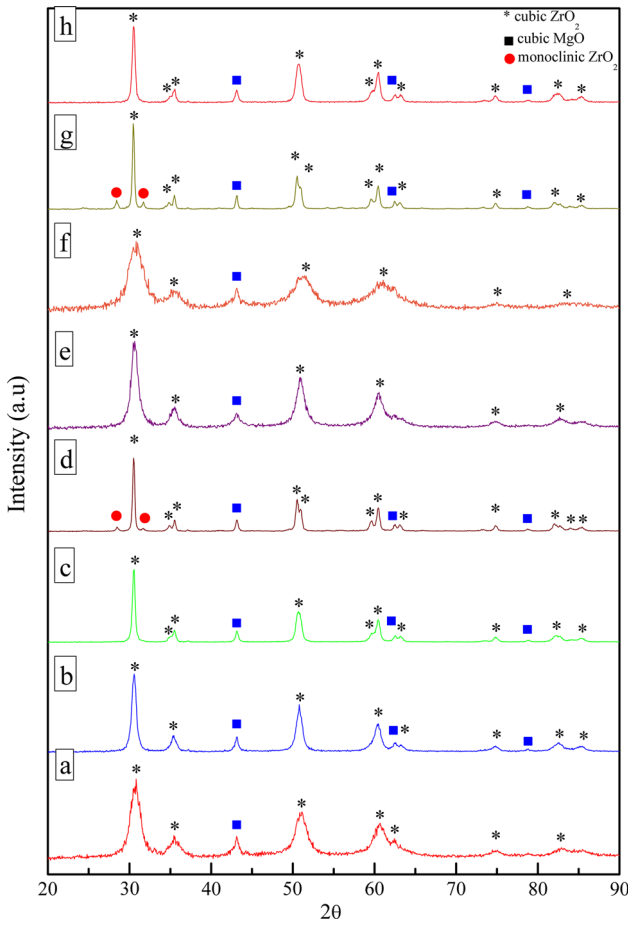

Fig. 5 X-ray diffraction pattern of samples *a* sample 1, *b* sample 2, *c* sample 3, *d* sample 4, *e* sample 5, *f* sample 6, *g* sample 7 and *h* sample 8

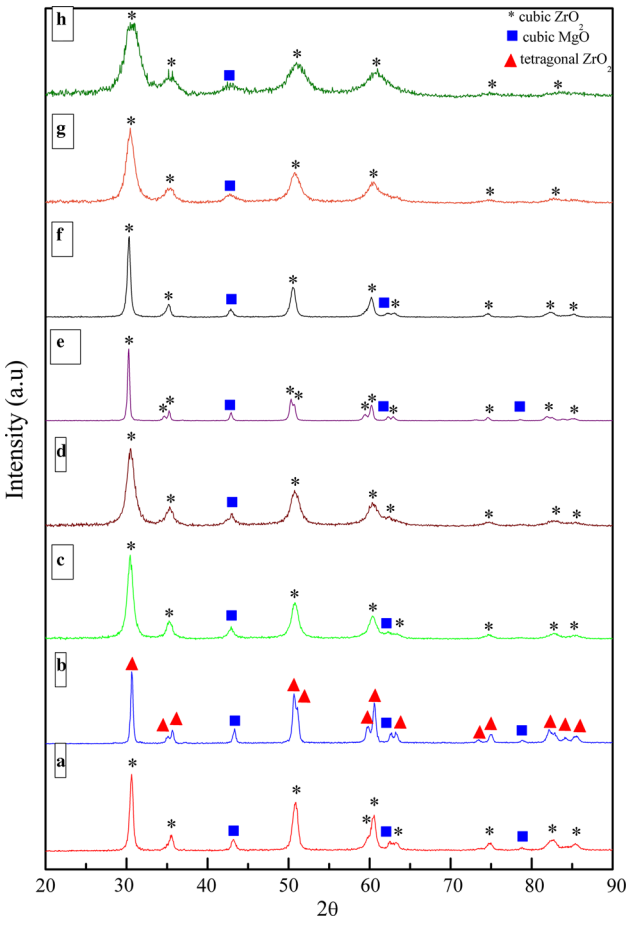

Fig. 6 X-ray diffraction pattern of samples *a* sample 9, *b* sample 10, *c* sample 11, *d* sample 12, *e* sample 13, *f* sample 14, *g* sample 16 and *h* sample 16

disorder, having a free energy, G_2 or G_3. This phase can then be used as a precursor to get the preferred chemical composition (other fewer metastable phases) and/or microstructure (e.g., nanocrystalline material) by following heat treatment/processing. It has been shown that materials processed in this way have improved physical and mechanical features in contrast to the conventional ingot (solidification) processed materials. These metastable phases can also be transformed to the equilibrium crystalline phase(s) by long-term annealing [46–50].

Departure of different processing techniques from equilibrium to synthesize non-equilibrium structures could be possibly different from each other. The capability of various processing techniques to synthesize non-equilibrium structures may be suitably estimated by measuring or approximating the achieved departure from equilibrium, i.e., the maximal energy that can be stored as well as that of the equilibrium/stable structure [51].

It has long been identified in the chemical literature that metastable oxide structures can be synthesized by the pyrolytic decomposition of hydroxides, salts or metal–organic compound solutions. Perhaps, the most notable example is the host of metastable aluminas that evolve from the pyrolysis of AL hydroxides between 300 and 1,000 °C [52]. In this study, the formation of tetragonal and monoclinic ZrO_2 in some cases and also, cubic MgO phase in all samples indicated that rapid solidification departure from equilibrium was more than the sol–gel process. In other words, Pechini sol–gel process for synthesizing MSZ nanoparticles was more near equilibrium state in comparison with the atmospheric plasma spray (APS) process.

3.3 Analysis of variance (ANOVA)

A Taguchi method was used to identify the optimal conditions and select the parameters having the most principal influence on the particle size of magnesia-stabilized zirconia nanoparticles. The optimum level of process could be gained by applying the standard analysis. Since the aim of experiments was to obtain the nearly spherical shape of

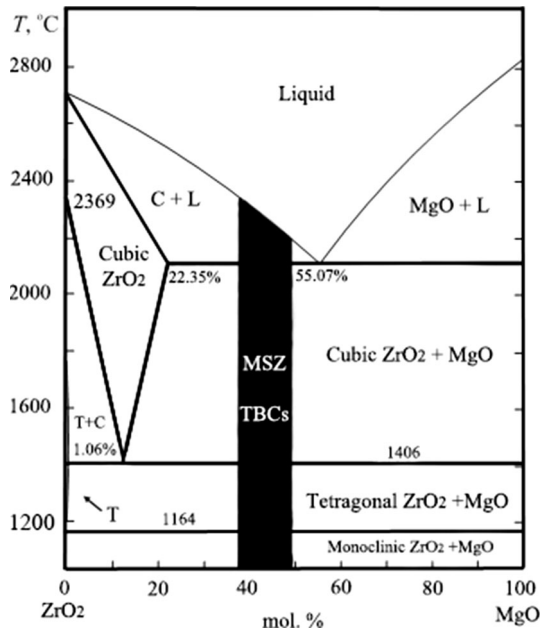

Fig. 7 ZrO_2–MgO phase diagram. According to the engineering guidelines presented in the literature, it is suggested that MSZ for thermal barrier applications (TBCs) should have compositions included within the *dark-shaded region*

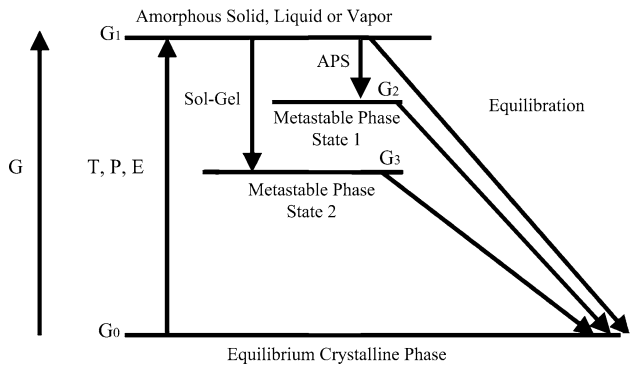

Fig. 8 The basic concept of "energize and quench" to synthesize non-equilibrium materials. Adopted from ref ([51])

Table 3 Table of main effects

Factor	Level 1	Level 2	Level 3	Level 4	L2 − L1
CA/EG	17.75	22.75	3	27	5
CA/TM	22.75	21.5	24.25	30	−1.25
Temperature	22.5	27.25	25.75	20	1.75
Time	22.5	25.75	21.75	–	0.25

particles and finer particles, standard analysis was chosen to be smaller as it was better for particle size, so standard analysis values were determined according to the Table 3.

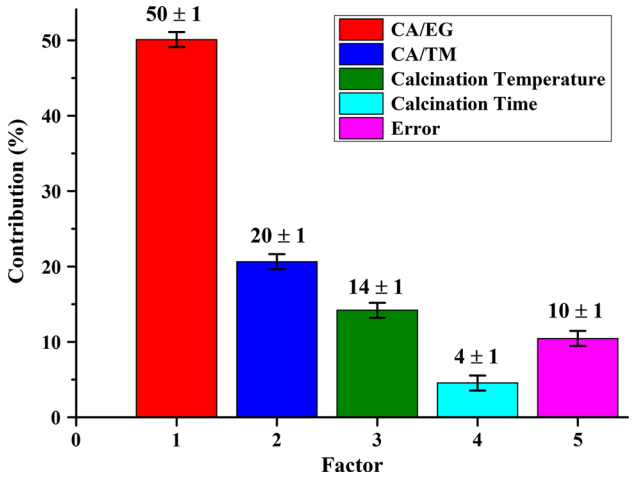

Fig. 9 Contribution percentage of each factor on the particle size

Figure 9 shows contribution percentage of each factor on the particle size. The most influential factor was CA/EG mole ratio, which contributed to the response by 50.109 percent. Other factors were CA/TM mole ratio, calcination temperature and time by the contribution of 20.633, 14.21, and 4.554 %, respectively. The error percentage of the experiment was 10.464 %, showing that the results were acceptable [53].

In the Taguchi optimization procedure [53, 54] the analysis of the experimental data using FE (factor effect) analysis and the ANOVA (analysis of variance) gave an output which was statistically significant in the outcome of the optimum synthesis condition. ANOVA was done using Qualitek-4 software on the one response variables. The results obtained have been tabulated in Table 4. The purpose of the analysis of variance (ANOVA) was to investigate which factors significantly affected the quality characteristic. In the Table 4, f signifies degree of freedom, S represents the sum of square of each column and V is the variance of factor. The significance of the control factors on characteristics can be estimated by the results of the ANOVA process. The significance means the extent of a control factor's effect on characteristics can be determined using the F values of the F-distribution. The F values are used to determine whether or not a control factor can be pooled to an error term. In general, the results of the experiments have a small degree of freedom and therefore, a pooling method is used to increase the freedom of error. In Table 4, factor C and D were deleted, implying that the lowest F value (FC = 7.791 and FD = 4.265) was combined ('pooled') with the error term. Therefore, factors A and B have some effect on particle size, but C and D have no significance. In particular, the calculated values for FA and FB are higher than FC and FD. High values for the

Table 4 The ANOVA table of mean particle size

Factor	Representation	DOF (f)	Sum of Sqrs (S)	Variance (V)	F-ratio (F)	Pure sum (S′)	Percent P (%)
CA/EG	A	3	388.25	129.416	24.947[a]	372.687	50.109
CA/TM	B	3	169.25	56.416	10.875[a]	153.687	20.663
Temperature	C	3	121.25	40.416	7.791	105.687	14.21
Time	D	2	44.25	22.125	4.265	33.875	4.554
Other/error		4	20.75	5.187	–	–	10.464
Total		15	743.75	–	–	–	100

[a] Most significant parameter

Table 5 Prediction for optimum sample

Factor	Optimum conditions	Level	Contribution
CA/EG	1	1	−6.875
CA/TM	2	2	−3.125
Calcination temperature (°C)	900	3	−4.625
Calcination time (h)	8	4	−2.875

Table 6 Results of the confirmation experiment for particle size

	Average particle size (nm)	
	Level	Particle size (nm)
Prediction	A1B2C4D3	7.125
Experiment	A1B2C4D3	5.6

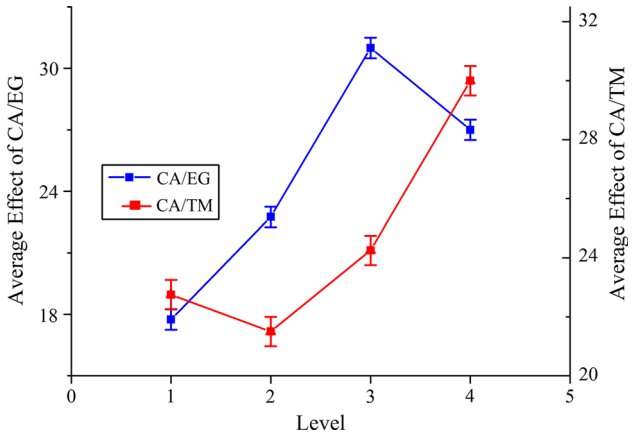

Fig. 10 Average effect (±0.5) plots of CA/EG mole ratio (*blue line*), CA/TM mole ratio on particle size of MSZ (*red line*) (Color figure online)

calculated Fi mean the greater influence of factor i on the experiment outcome. The calculated F values for A (24.947) and B (10.875) were both higher than the identification value F, implying that these parameters had the most significant influence on the result of the experiment.

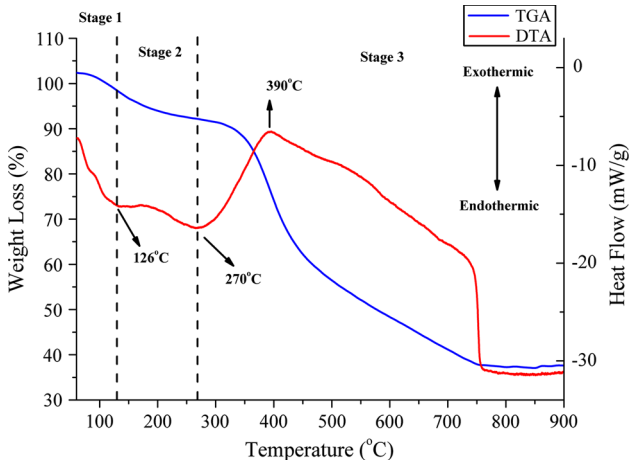

Fig. 11 TGA-DTA analysis of dried gel for the optimum sample, in static atmosphere air between 30 and 900 °C, with a heating rate of 5 °C min^{-1}

3.4 Estimation and approval of properties

After setting the data on Qualitek-4 software, the optimum MSZ sample, which was preferred to be nearly spherical shape and with finer particle size, was determined. According to the results obtained from software, citric acid to ethylene glycol mole ratio (CA/EG) must be equal to 1 and citric acid to transition metal mole ratio (CA/TM) should be 2. Calcinations temperature and time were found to have no main effects on the particle size of the samples (Table 5). Given the fact that the sample with such characters did not exist among the sixteen samples synthesized according to the M_{16} array, the sample with these optimum conditions was synthesized.

When the optimal level of the design parameters was carefully chosen, the last step was to forecast and validate the perfection of the quality characteristic using the optimal level of the design parameters [53].

The expected result at optimum conditions was 7.125 nm for particle size. Table 6 shows the comparison of the predicted particle size with the experimental results using the optimal conditions. There was a good agreement between the predicted and experimental particle size.

Consequently, particle size in the synthesis of MSZ nanoparticles can be improved through the Taguchi method approach.

3.5 The effect of different parameters on the particle size

Figure 10 shows the average effect of each factor on particle size. In accordance with Fig. 10 (the blue line), increasing CA/EG from one to four increased the average effect of this factor on the particle size. Consistent with this diagram, at the first, increasing the CA/EG mole ratio caused the fast increase of the average effect and then this increase fell down gradually. The minimum amount of the average effect on smaller particle was related to the CA/EG = 1 value, which indicated that the optimum amount for this parameter was 1. Such a difference in particle size was probably due to the homogeneity of cations in the resin structure, which was influenced by the CA/EG ratio. Indeed, in the Pechini process, the general idea of the process is to obtain a polymer precursor involving randomly coiled macromolecular chains, throughout which the metal cations are uniformly distributed on an atomic level. Laberty-Robert et al., for the synthesis of nanocrystalline ZrO_2–8 $\%Y_2O_3$ via a polymerization route, reported that there was a reverse relationship between CA/EG mole ratio and the viscosity of sol. When the CA/EG ratio was low, the viscosity of the sol was high. The low mobility of metal cations in the highly viscous polymeric resin (the lower CA/EG mole ratio) could inhibit the metal cations from forming mixed metal–oxides bonds before pyrolysis. Hence, the solid ceramic would be formed only after the organic network is eliminated. This may affect the crystallization temperature of the oxide to the higher temperatures and as a consequence, the higher CA/EG mole ratio causes the smaller particle sizes. Once the CA/EG ratio is increased, the agglomerate size in the resultant powder becomes greater and also, the structure turns out to be denser; there is a tendency for the partial sintering of the crystallites. Furthermore, in the synthesis of ZrO_2–CeO_2 powder by the use of polymeric precursor based on Pechini process, Quinelato et al. [41] reported that the decrease of the CA/EG ratio (increase of ethylene glycol amount) favored the decrease in particle size. Increasing the amount of ethylene glycol caused an increase in the polymeric chain length, thereby increasing the distance between chelated cations. This phenomenon proposes that the weaker interactions among the primary particles happen throughout crystallization, thus leading to the smaller particle sizes.

The average effect of CA/TM mole ratio has been illustrated in Fig. 10 (the red line). Overall, the effect of this factor was increased by increasing the ratio from one to four. The minimum effect for this parameter belonged to the CA/TM = 2 mol ratio. It was found by Laberty-Robert et al. that if the CA/TM ratio were high, the viscosity of the solution would also be high; in fact there was a direct association between CA/TM ratio and the viscosity of the sol. In the hydroxycarboxylic acid, the acid purposes include:

- The uniform distribution of cations over the polymeric chains by chelation of the metal cations.

Or

- Formation of organic esters by the reaction with the alcohol function of the polyhydroxyalcohol.

Consequently, after the CA/TM ratio is increased, the amount of hydroxycarboxylic acid which can react with polyhydroxyalcohol is more substantial. Then, in the solution, the polymeric chains are more important, and/or branched or longer. This encourages a reduction in the mobility of the polymeric chains and leads to an increase in the viscosity. Hence, similar to the explanations proposed for the CA/EG mole ratio, the increase of CA/TM mole ratio may also cause smaller particle sizes.

Furthermore, calcination temperature and time parameters have the lowest effectiveness on MSZ fabrication in comparison to the two previously discussed variables and can be pooled to error in respect to the Taguchi manner of design (Table 4).

3.6 Characterization of the optimum synthesized sample

3.6.1 TGA and DTA analysis

To determine the best annealing conditions for the crystallization temperature of MSZ phases and also investigate the thermal behavior of the precursor gel, thermal analyses were performed. Thermogravimetric and differential thermal analysis (TG/DTA) profiles of the dried gel for MSZ optimum sample under air atmosphere are given in Fig. 11. As can be clearly seen in Fig. 11, degradation of polymeric network is a multi-step process completed at temperatures of about 800 °C. The overall weight loss (TG) and energy change (DTA) took place in three steps. According to the TG curve, the total weight loss was about 65 % of the total precursor mass, along with two endothermic and one broad exothermic peak observed in DTA. The first stage of weight loss, which was about 10 wt%, occurred at the temperature range of 25–126 °C, corresponding to the first endothermic peak shown by DTA curve. It could be assigned to the removal and evaporation of physically absorbed or trapped water molecules. Another peak seen at 270 °C was associated with two probable different

reactions, one was the dehydration of magnesium–zirconium hydroxide and the other one was extra ethylene glycol evaporation from the dried gel. By considering that the elimination of organics through both oxidation and crystallization were exothermic reactions, one broad and strong exothermic peak which appeared in the range 350–760 °C (step 3) was assigned to the oxidative decomposition of the polymeric metal–carboxylate or combustion of the chelate complex along with the formation of metal oxides, decomposition of magnesium nitrate and finally, crystallization of the ZrO_2 and MgO crystalline structures from the amorphous gel network [55]. Given that the thermal stability of polymeric network can efficiently prevent the aggregation of powders at high temperatures of calcination, it may be expected that gel decomposition happens to a large extent with a weight loss of about 65 percent [20].

3.6.2 XRD analysis

XRD analysis of optimum sample shown in Fig. 12 indicated that some peaks could be attributed to metastable tetragonal ZrO_2, and others to the cubic MgO. Close observation of Fig. 12 revealed the appearance of a peak at 43.3, which was the main peak of MgO structure.

The assignment of cubic and tetragonal structures, based only on the X-ray diffraction analysis, can be misleading because the cubic and tetragonal structures ($a_0 = 0.5124$ nm for cubic, and $a_0 = 0.5094$ nm and $c_0 = 0.5177$ nm for tetragonal structures) are very similar. Srivastava et al. [56] reported that the tetragonal structure can be distinguished from the cubic structure by the presence of the characteristic splittings of the tetragonal phase, such as (002) (200), (113) (311), (004) (400), (006) (600), etc., whereas the cubic phase exhibits only single peaks at all these positions. Garvie et al. [57] utilized high-angle reflections to distinguish the cubic and tetragonal structures and determine their relative proportions. In an investigation of plasma-sprayed yttria stabilized zirconia coatings, Miller et al. [58] used the (400) region of the X-ray diffraction patterns in order to calculate the relative proportions of cubic and tetragonal phases. They reported that the dominant peaks in this region were changed from the monoclinic to tetragonal and gradually, to the cubic reflections with an increase in the level of yttria. A "curve resolver" was used to separate the tetragonal and cubic peak components in the (400) region and the d values for the (400) and (004) tetragonal peaks were calculated from the curve-resolved peak positions [56].

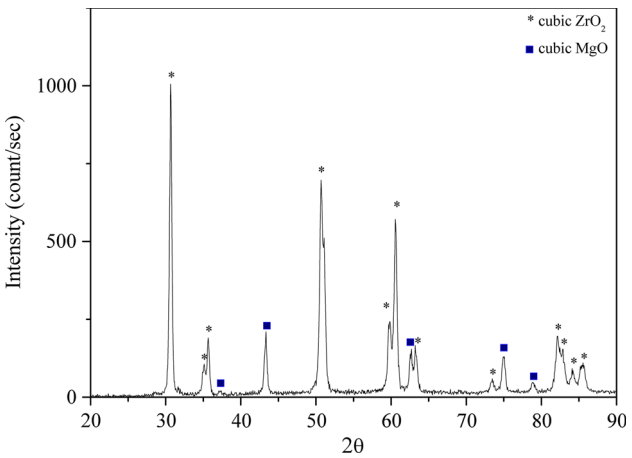

Fig. 12 XRD pattern of MSZ nanoparticles obtained at optimal conditions

3.6.3 Raman analysis

Raman spectroscopy was used to further investigate the crystal structure of optimum MSZ sample, as X-ray would give little information on the oxygen lattice. Raman

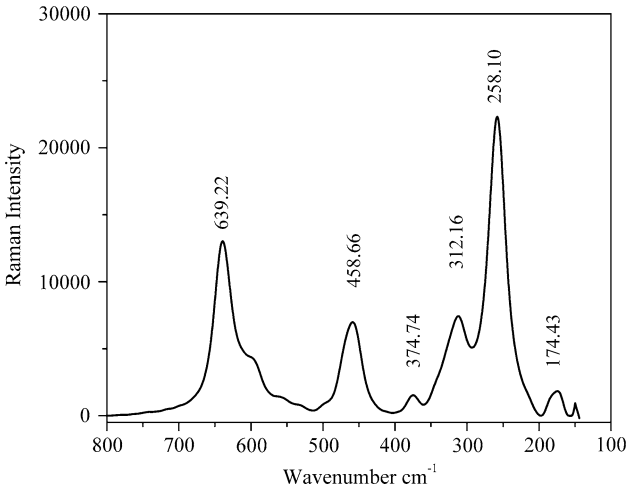

Fig. 13 Raman spectroscopy of optimum sample at wavenumber range of 100–800 cm^{-1}

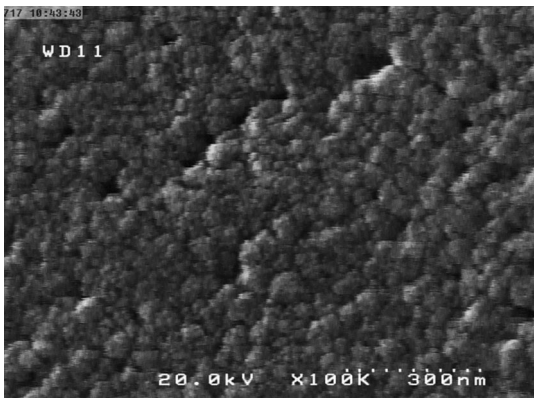

Fig. 14 FESEM photograph of the MSZ powder prepared by Pechini method showing secondary near spherical particles

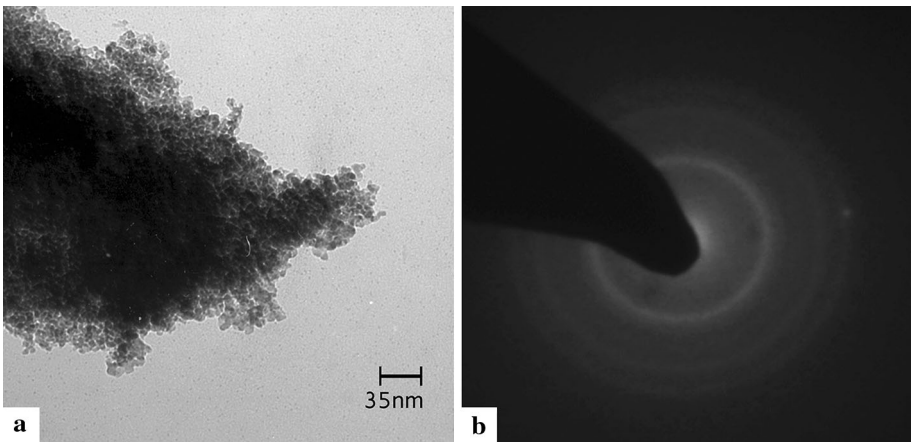

Fig. 15 TEM images and electron diffraction patterns of MSZ calcined at 900 °C for 8 h: **a** bright field image of primary particles and **b** electron diffraction pattern of the same sample

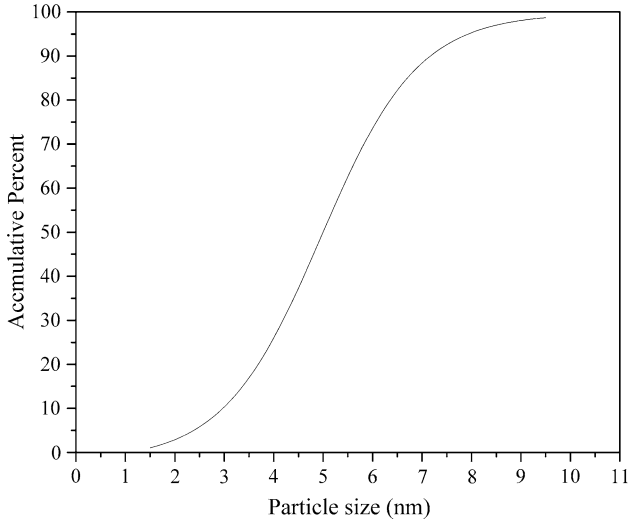

Fig. 16 Particle size distributions for the optimum sample

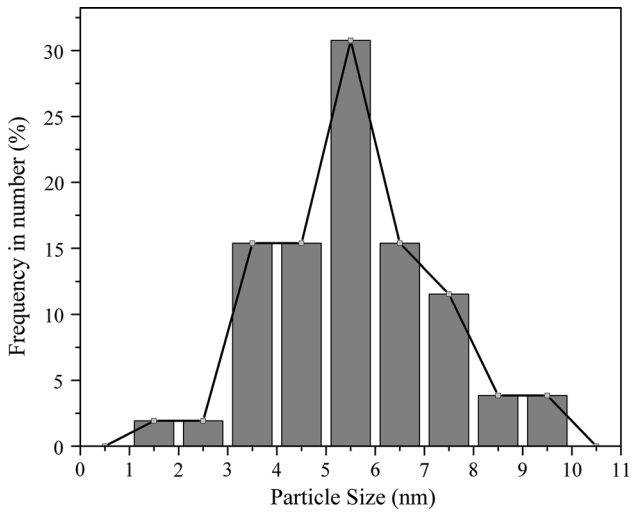

Fig. 17 Frequency number of optimum sample at different particle size ranges

spectroscopy allows the study of the anion sublattice structure and therefore, the structure of the solid solution phases [22, 23]. It is worthwhile to mention that Raman measurements were performed at a much shorter measuring interval and did not require any special sample preparation, compared to XRD. The Raman spectrum for optimum sample is shown in Fig. 13. In the case of magnesium substitution, since the tetragonal symmetry has only six active modes [21], the associated peaks are reported in Fig. 13. For each powder, no mixture with a monoclinic phase was observed. This was in perfect agreement with the XRD analysis.

3.6.4 FE-SEM and TEM analysis

The FESEM and TEM micrograph and particle size distribution of the MSZ nanoparticles obtained at optimal conditions brought in Table 5 are shown in Figs. 14, 15, 16 and 17, respectively. The MSZ nanoparticles with a particle size of 5.6 nm were prepared, as shown in Fig. 15a. The particle size distribution of the powder was also

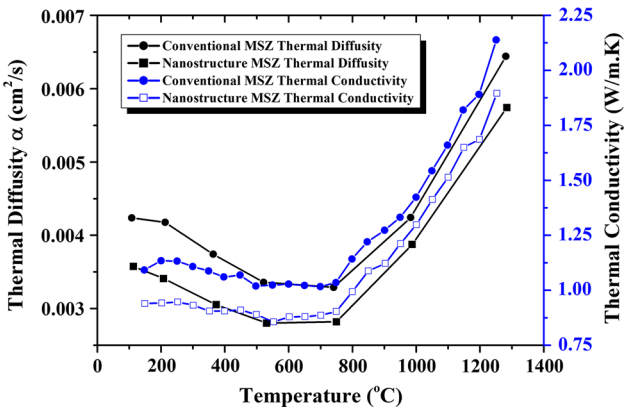

Fig. 18 Thermal diffusivity α(T) and thermal conductivity K(T) results of the conventional [60] and nanostructured MSZ

Table 7 Average effect of different factors on particle size

	CA/EG	CA/TM	Temperature	Time
Level 1	17.75	22.75	25.5	25
Level 2	22.75	21.5	27.25	25.75
Level 3	31	24.25	25.75	21.75
Level 4	27	30	20	–

measured with TEM images. It was found that the broad particle size distribution of MSZ nanoparticles was prepared. The average secondary particle size, which was estimated from FESEM micrographs, was around 18.82 nm, thereby not complying with TEM results and indicating that particles observed in TEM were the primary particles (Fig. 15). FESEM studies confirmed the presence of agglomerates in the sample. However, overall MSZ powder displayed a low agglomerated microstructure with homogeneous particle size distribution (Figs. 16, 17).

3.6.5 Thermal diffusivity α(T) and conductivity K(T)

The variation in thermal diffusivity and thermal conductivity values of conventional MSZ [59] and nano-MSZ from room temperature to 1,300 °C are presented in Fig. 18. In both MSZ significant increase of α(T) was observed at the temperature range of 800–1,300 °C. This was predominantly caused by the precipitation of the MgO from the zirconia matrix leading to unstabilization of the cubic/tetragonal zirconia (c/t–ZrO_2 to m–ZrO_2). Furthermore, at high temperatures, radiative heat transfer through the material in the course of the thermal diffusivity measurement might lead to this apparent increase [59].

It can be seen that both thermal diffusivity and thermal conductivity of nanostructured MSZ is lower than conventional MSZ reported in literature [60].

The phonon mean path can be given by

$$\frac{1}{l} = \frac{1}{l_i} + \frac{1}{l_p} + \frac{1}{l_b} \quad (1)$$

where phonon mean path due to inherent conductivity, point defect scattering and grain-boundary scattering are l_i, l_p and l_b, respectively. In nanostructured MSZ, grain-boundary scattering also has a significant effect on phonon mean path, which can be described by [61]

$$\frac{1}{l_b} = \frac{T\gamma^2}{20T_m\alpha} \quad (2)$$

where T_m is the absolute melting temperature, α is the lattice constant, and γ is the Gruneisen constant. Using the Eq. (2), grain-boundary scattering calculated for single crystal of MSZ as 32 nm.

The grain size of MSZ is 20–30 nm, which is comparable to phonon mean free path owing to grain boundary scattering. The small grain size leads in lower thermal conductivity owing boundary thermal resistance endorsed by phonon scattering at grain boundaries [62, 63] (Table 7).

4 Conclusion

Magnesia-stabilized zirconia nanoparticles with a metastable tetragonal zirconia and a stable cubic magnesia phase constituent was successfully synthesized by Pechini sol–gel type method. M_{16} orthogonal array of Taguchi method was employed to optimize experimental settings for the synthesis of magnesia-stabilized zirconia nanoparticles. Consequently, citric acid to ethylene glycol mole ratio (CA/EG) and citric acid to transition metal mole ratio (CA/TM) were found to be the main parameters having a significant effect on particle size and the size distribution of magnesia-stabilized zirconia nanoparticles, respectively. In optimal conditions of this method, magnesia-stabilized zirconia nanoparticles (5.6 nm) with homogeneous particle size distribution were prepared and the results were in a good agreement with the predicted data as examined by Taguchi method. Furthermore, in Pechini sol–gel process, for synthesizing MSZ nanoparticles, it was found out that the formation of the tetragonal and monoclinic ZrO_2 in some cases and also, the cubic MgO phase in all samples indicated that the departure of the rapid solidification from equilibrium was more than that of the sol–gel process. Furthermore, the thermal conductivity and diffusivity of nano-MSZ are lower than that of traditional magnesia-stabilized zirconia.

Acknowledgments The authors would like to thank Malek Ashtar University of Technology (MUT) for financially support of this research.

References

1. Nelson WA, Orenstein RM (1997) TBC experience in land-based gas turbines. J Therm Spray Technol 6(2):176–180
2. Schulz U, Fritscher K, Peters M (1996) EB-PVD Y_2O_3-and $CeO_2Y_2O_3$-stabilized zirconia thermal barrier coatings—crystal habit and phase composition. Surf Coat Technol 82(3):259–269
3. Bennett A (1986) Properties of thermal barrier coatings. Mater Sci Technol 2(3):257–261
4. Brandon J, Taylor R (1989) Thermal properties of ceria and yttria partially stabilized zirconia thermal barrier coatings. Surf Coat Technol 39:143–151
5. Steffens H-D, Fischer U (1987) Characterization and thermal shock testing of Yttria-stabilized zirconia coatings. Surf Coat Technol 32(1):327–338

6. Nusair Khan A, Khan S, Ali F, Iqbal M (2009) Evaluation of ZrO_2–24MgO ceramic coating by eddy current method. Comput Mater Sci 44(3):1007–1012
7. Strangman TE (1985) Thermal barrier coatings for turbine airfoils. Thin Solid Films 127(1):93–106
8. Kvernes I (1979) Ceramic coatings on diesel engine components. In: Kvernes I et al (eds) Central Institute for Industrial Research, Oslo, Norway, Dec 1979. From conference on advanced materials for alternate fuel capable directly fired heat engines, pp 233–257
9. Jamali H, Mozafarinia R, Shoja-Razavi R, Ahmadi-Pidani R (2014) Comparison of hot corrosion behaviors of plasma-sprayed nanostructured and conventional YSZ thermal barrier coatings exposure to molten vanadium pentoxide and sodium sulfate. J Eur Ceram Soc 34(2):485–492
10. Lima R, Marple B (2008) Toward highly sintering-resistant nanostructured ZrO_2–7wt.% Y_2O_3 coatings for TBC applications by employing differential sintering. J Therm Spray Technol 17(5–6):846–852
11. Zhu D, Miller RA (2004) Development of advanced low conductivity thermal barrier coatings. Int J Appl Ceram Technol 1(1):86–94
12. Chatterjee M, Chatterjee A, Ganguli D (1992) Preparation of ZrO_2·CaO and ZrO_2·MgO fibres by alkoxide sol–gel processing. Ceram Int 18(1):43–49
13. Settu T (2000) Characterisation of MgO–ZrO_2 precursor powders prepared by in situ peptisation of coprecipitated oxalate gel. Ceram Int 26(5):517–521
14. Muccillo R, Saito N, Muccillo E (1995) Properties of zirconia–magnesia solid electrolytes prepared by the citrate method. Mater Lett 25(3):165–169
15. Gocmez H, Fujimori H (2008) Synthesis and characterization of ZrO_2–MgO solid solutions by citrate gel process. Mater Sci Eng B 148(1):226–229
16. Kim N, Hsieh C-H, Huang H, Prinz FB, Stebbins JF (2007) High temperature ^{17}O MAS NMR study of calcia, magnesia, scandia and yttria stabilized zirconia. Solid State Ion 178(27):1499–1506
17. Balmer ML, Lange FF, Levi CG (1992) Metastable phase selection and partitioning in ZrO_2—MgO processed from liquid precursors. J Am Ceram Soc 75(4):946–952
18. Muccillo E, Rocha R, Muccillo R (2002) Preparation of Gd_2O_3-doped ZrO_2 by polymeric precursor techniques. Mater Lett 53(4):353–358
19. Kim KD, Choi DW, Choa Y-H, Kim HT (2007) Optimization of parameters for the synthesis of zinc oxide nanoparticles by Taguchi robust design method. Colloids Surf A 311(1):170–173
20. Oghaz MH, Razavi RS, Estark ML, Ghasemi R (2013) Optimization of morphology and particle size of modified sol–gel synthesized YSZ nanopowder using Taguchi method. J Nano Res 21:65–70
21. Kim SM, Park KS, Kim KD, Park SD, Kim HT (2009) Optimization of parameters for the synthesis of bimodal Ag nanoparticles by Taguchi method. J Ind Eng Chem 15(6):894–897
22. Sadat-Shojai M, Khorasani M-T, Jamshidi A (2012) Hydrothermal processing of hydroxyapatite nanoparticles—a Taguchi experimental design approach. J Cryst Growth 361:73–84
23. Norouzbeigi R, Edrissi M (2011) Modification and optimization of nano-crystalline Al_2O_3 combustion synthesis using Taguchi L_{16} array. Mater Res Bull 46(10):1615–1624
24. Hou T-H, Su C-H, Liu W-L (2007) Parameters optimization of a nano-particle wet milling process using the Taguchi method, response surface method and genetic algorithm. Powder Technol 173(3):153–162
25. Akhgar B, Pazouki M, Ranjbar M, Hosseinnia A, Salarian R (2012) Application of Taguchi method for optimization of synthetic rutile nano powder preparation from ilmenite concentrate. Chem Eng Res Des 90(2):220–228
26. Chou C-S, Wu C-Y, Yeh C-H, Yang R-Y, Chen J-H (2012) The optimum conditions for solid-state-prepared $(Y_{3-x}Ce_x)$ Al_5O_{12} phosphor using the Taguchi method. Adv Powder Technol 23(1):97–103
27. Kim KD, Kim SH, Kim HT (2005) Applying the Taguchi method to the optimization for the synthesis of TiO_2 nanoparticles by hydrolysis of TEOT in micelles. Colloids Surf A 254(1):99–105
28. Shamsipur M, Pourmortazavi SM, Hajimirsadeghi SS, Roushani M (2013) Applying Taguchi robust design to the optimization of synthesis of barium carbonate nanorods via direct precipitation. Colloids Surf A Physicochem Eng Asp 423:35–41
29. Biabani A, Rezaei M, Fattah Z (2012) Optimization of preparation conditions of Fe–Co nanoparticles in low-temperature CO oxidation reaction by taguchi design method. J Nat Gas Chem 21(4):415–420
30. Pourmortazavi SM, Hajimirsadeghi SS, Rahimi-Nasrabadi M, Zahedi MM (2012) Taguchi robust design to optimize synthesis of lead oxalate nano-disks. Mater Sci Semicond Process 16(1):131–137
31. Kim KD, Han DN, Kim HT (2004) Optimization of experimental conditions based on the Taguchi robust design for the formation of nano-sized silver particles by chemical reduction method. Chem Eng J 104(1):55–61
32. Abrishamkar M, Azizi SN, Kazemian H (2011) Using Taguchi robust design method to develop an optimized synthesis procedure for nanocrystals of ZSM-5 zeolite. Zeitschrift für anorganische und allgemeine Chemie 637(1):154–159
33. Edrissi M, Norouzbeigi R (2008) Taguchi optimization for combustion synthesis of aluminum oxide nano-particles. Chin J Chem 26(8):1401–1406
34. Norouzbeigi R, Edrissi M (2011) Preparation of nano alumina powder via combustion synthesis: porous structure optimization via taguchi L16 design. J Am Ceram Soc 94(11):4052–4058
35. Shadpour H, Edrissi M, Zanjanchi MA (2002) Preparation and characterization of CoxMnmCrnNikFe3-(x + m + n + k) O4 ferrites and optimization of their structural and magnetic properties by Taguchi experimental design. J Mater Sci Mater Electron 13(3):139–148
36. Montgomery DC, Montgomery DC, Montgomery DC (1997) Design and analysis of experiments, vol 7. Wiley, New York
37. Laberty-Robert C, Ansart F, Deloget C, Gaudon M, Rousset A (2001) Powder synthesis of nanocrystalline ZrO_2–8%Y_2O_3 via a polymerization route. Mater Res Bull 36(12):2083–2101. doi:10.1016/S0025-5408(01)00723-1
38. Laberty-Robert C, Ansart F, Castillo S, Richard G (2002) Synthesis of YSZ powders by the sol–gel method: surfactant effects on the morphology. Solid State Sci 4(8):1053–1059
39. Lessing PA (1989) Mixed-cation oxide powders via polymeric precursors. Am Ceram Soc Bull 68(5):1002–1007
40. Tai L-W, Lessing PA (1992) Modified resin-intermediate processing of perovskite powders: part I. Optimization of polymeric precursors. J Mater Res 7(2):502–510
41. Quinelato A, Longo E, Leite E, Bernardi M, Varela J (2001) Synthesis and sintering of ZrO_2–CeO_2 powder by use of polymeric precursor based on Pechini process. J Mater Sci 36(15):3825–3830
42. Jones RL (1996) Experiences in seeking stabilizers for zirconia having hot corrosion-resistance and high temperature tetragonal (t') stability. DTIC document
43. Buyakova S, Promakhov V, Kulkov S (2012) Thermal tests and their effect on the micro-and macrostructure of nanocrystalline ZrO2. Powder Metall Met Ceram 51(5–6):267–272
44. Meier SM, Gupta DK, Sheffler KD (1991) Ceramic thermal barrier coatings for commercial gas turbine engines. JOM 43(3):50–53
45. Martin G, Bellon P (1996) Driven alloys. Solid State Phys 50:189–331

46. Lipkin DM, Krogstad JA, Gao Y, Johnson CA, Nelson WA, Levi CG (2013) Phase evolution upon aging of air-plasma sprayed t′-zirconia coatings: I—synchrotron X-ray diffraction. J Am Ceram Soc 96(1):290–298
47. Brandont J, Taylor R (1991) Phase stability of zirconia-based thermal barrier coatings Part I. Zirconia–yttria alloys. Surf Coat Technol 46:75–90
48. Rebollo NR, Gandhi AS, Levi CG (2003) Phase stability issues in emerging TBC systems. High Temp Corros Mater Chem IV 2003:431–442
49. Leoni M, Jones R, Scardi P (1998) Phase stability of scandia–yttria-stabilized zirconia TBCs. Surf Coat Technol 108:107–113
50. Langjahr PA, Oberacker R, Hoffmann MJ (2001) Long-term behavior and application limits of plasma-sprayed zirconia thermal barrier coatings. J Am Ceram Soc 84(6):1301–1308
51. Suryanarayana C (2004) Mechanical alloying and milling. CRC Press, Boca Raton
52. Jayaram V, De Graef M, Levi C (1994) Metastable extension of the fluorite phase field in Y_2O_3·ZrO_2 and its effect on grain growth. Acta Metall Mater 42(6):1829–1846
53. Taguchi G (1986) Introduction to quality engineering: designing quality into products and processes. ARRB Group Limited
54. Fowlkes WY, Creveling CM, Derimiggio J (1995) Engineering methods for robust product design: using Taguchi methods in technology and product development. Addison-Wesley, Reading
55. Tian X, Zeng Y, Xiao T, Yang C, Wang Y, Zhang S (2011) Fabrication and stabilization of nanocrystalline ordered mesoporous MgO–ZrO_2 solid solution. Microporous Mesoporous Mater 143(2):357–361
56. Srinivasan R, De Angelis RJ, Ice G, Davis BH (1991) Identification of tetragonal and cubic structures of zirconia using synchrotron x-radiation source. J Mater Res 6(6):1287–1292
57. Garvie R, Hannink R, Pascoe R (1975) Ceramic steel? Nature 258:703–704
58. Miller RA, Berndt CC (1984) Performance of thermal barrier coatings in high heat flux environments. Thin Solid Films 119(2):195–202
59. Clarke DR (2003) Materials selection guidelines for low thermal conductivity thermal barrier coatings. Surf Coat Technol 163:67–74
60. Ahmaniemi S, Vuoristo P, Mäntylä T, Cernuschi F, Lorenzoni L (2004) Modified thick thermal barrier coatings: thermophysical characterization. J Eur Ceram Soc 24(9):2669–2679
61. Soyez G, Eastman JA, Thompson LJ, Bai G-R, Baldo PM, McCormick AW, DiMelfi RJ, Elmustafa AA, Tambwe MF, Stone DS (2000) Grain-size-dependent thermal conductivity of nanocrystalline yttria-stabilized zirconia films grown by metal-organic chemical vapor deposition. Appl Phys Lett 77(8):1155–1157
62. Rauf A, Yu Q, Jin L, Zhou C (2012) Microstructure and thermal properties of nanostructured lanthana-doped yttria-stabilized zirconia thermal barrier coatings by air plasma spraying. Scripta Mater 66(2):109–112
63. Guo X (1997) Space-charge conduction in yttria and alumina codoped-zirconia 1. Solid State Ion 96(3):247–254